

Dynamics of hyperthermal $\text{Kr}^{++}\text{H}_2\text{O}$ charge transfer collisions

Susan T. Arnold, Rainer A. Dressler, Michael J. Bastian, James A. Gardner, and Edmond Murad

Citation: *The Journal of Chemical Physics* **102**, 6110 (1995); doi: 10.1063/1.469345

View online: <http://dx.doi.org/10.1063/1.469345>

View Table of Contents: <http://scitation.aip.org/content/aip/journal/jcp/102/15?ver=pdfcov>

Published by the AIP Publishing

Articles you may be interested in

Charge transfer dynamics in ion–polyatomic molecule collisions: $\text{X}^{++}\text{H}_2\text{O}$ ($\text{X}=\text{N}, \text{Kr}$) luminescence study
J. Chem. Phys. **103**, 9989 (1995); 10.1063/1.469888

Competitive charge–transfer and vibrational quenching of $\text{N}^+ 2$ ($\text{X}, v=1$) in collisions with O_2 and NO
J. Chem. Phys. **89**, 1445 (1988); 10.1063/1.455696

Charge transfer collisions for polarized ion sources
AIP Conf. Proc. **117**, 180 (1984); 10.1063/1.34609

Selective excitation in charge transfer collisions with Ne_2
Appl. Phys. Lett. **29**, 108 (1976); 10.1063/1.88987

Crossed molecular beam study of the kinematics and dynamics of charge transfer collisions
J. Chem. Phys. **61**, 2720 (1974); 10.1063/1.1682405



Dynamics of hyperthermal $\text{Kr}^+ + \text{H}_2\text{O}$ charge-transfer collisions

Susan T. Arnold,^{a)} Rainer A. Dressler, Michael J. Bastian,^{b)} James A. Gardner,^{c)} and Edmond Murad

Phillips Laboratory, Spacecraft Interactions Branch, PL/WSSI, Hanscom Air Force Base, Massachusetts 01731-3010

(Received 29 November 1994; accepted 12 January 1995)

Cross section, time-of-flight (TOF) and luminescence measurements are reported for the $\text{Kr}^+ + \text{H}_2\text{O}$ charge-transfer system. Cross section and TOF measurements were carried out in an octopole guided-ion beam apparatus and are reported for collision energies between 0.10–10 eV (c.m.). The charge-transfer cross section has approximately an $E^{-0.5}$ dependence at low collision energies. TOF measurements of H_2O^+ products are characteristic of a near-resonant direct charge-transfer mechanism proceeding at long range. A smaller contribution of forward-scattered ions is attributed to the formation of longer-lived collision complexes. The TOF analysis based on the osculating complex model reveals significant energy transfer for orbiting trajectories. Low resolution product ion luminescence spectra (4 nm FWHM), taken at collision energies between 0.1–15 eV (c.m.), are consistent with the TOF measurements. The optical spectra show that H_2O^+ product ions are formed in \tilde{A} -state vibrational levels that are at or below the energy level of $\text{Kr}^+(^2P_{1/2})$ reactants. No evidence is found for luminescence stemming from $\text{Kr}^+(^2P_{3/2})$ reactants. © 1995 American Institute of Physics.

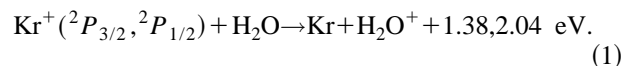
I. INTRODUCTION

Exothermic ion–molecule charge-transfer reactions at hyperthermal collision energies have been shown to be governed by two criteria.^{1,2} (1) energy resonance between reactant and product internal energies, and (2) Franck–Condon overlap between the reactant and product vibrational wave functions. The energy resonance criterion is in part a consequence of the fact that the nonadiabatic coupling inducing charge transfer is significant at long range. Thus the largest state-to-state charge-transfer cross sections are usually associated with large-impact parameter collisions with little energy transfer. A large Franck–Condon factor signifies that the multidimensional long-range potential energy surfaces of the reactants and products either exhibit a crossing seam or nearly overlap at energies in the vicinity of the respective reactant and product vibrational levels.

Examining the role of these two criteria in ion– H_2O charge-transfer reactions has been the focus of several reports by this laboratory,^{3–10} as hyperthermal charge-transfer collisions between atmospheric ions and H_2O are a major source of ionization in the environment of low-earth orbiting spacecraft.^{11,12} In particular, charge-transfer cross sections and product ion internal energy distributions were reported for the collision systems $\text{X}^+ + \text{H}_2\text{O}$, where $\text{X}^+ = \text{O}^+, ^{7,8} \text{Ar}^+, ^{6,9} \text{N}_2^+, ^{6,9}$ and $\text{N}^+.$ ^{4,10} The $\text{Ar}^+ + \text{H}_2\text{O}$ and $\text{N}_2^+ + \text{H}_2\text{O}$ charge-transfer collision systems provided particularly good insight into the charge-transfer dynamics due to the observation of intense $\text{H}_2\text{O}^+ \tilde{A} \ ^2A_1 - \tilde{X} \ ^2B_1$ charge-transfer luminescence.^{5,6} These systems are exothermic by ~ 3 eV and generally adhere to both energy resonance and Franck–Condon criteria. Both charge-transfer systems exhibit large hyperthermal cross sections. The luminescence analysis and

the product ion time-of-flight (TOF) studies⁹ demonstrate that the internal excitation of the products is governed by the respective exothermicities of the charge-transfer reactions, and that primarily bending vibrational levels of the \tilde{A} state are populated, in accordance with the fact that only the bending vibrational coordinate of that state exhibits significant Franck–Condon overlap with the reactant vibrational motion. (The energy dependence of the Franck–Condon overlap is obtained from the photoelectron spectrum of H_2O).^{13–15} In contrast, the $\text{N}^+ + \text{H}_2\text{O}$ charge-transfer reaction is not as efficient as expected considering the favorable Franck–Condon overlap at resonance. It is suggested that this discrepancy is due to a weaker electronic coupling with the product $\text{H}_2\text{O}^+ \tilde{A}$ -state surface.¹⁰ The $\text{O}^+ + \text{H}_2\text{O}$ collision system, which is exothermic by only ~ 1 eV, appears to violate the Franck–Condon criterion. In this system, the ground state energy level has essentially zero Franck–Condon overlap with product states at resonance. Nevertheless, the charge-transfer system exhibits large hyperthermal cross sections, and at least 90% of the H_2O^+ product ions are formed with internal energies near resonance.^{7,8}

In order to further clarify the different behavior of the various reactant ions, we continue our investigation of ion– H_2O hyperthermal charge-transfer reactions with the study of the $\text{Kr}^+ + \text{H}_2\text{O}$ system



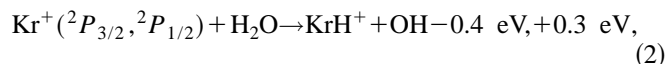
Due to the high ion–neutral mass ratio, this collision system permits beam experiments at very low center-of-mass energies with high sensitivity. Thus effects due to complex formation can be observed over a wide range of energies. Whereas only weak Franck–Condon overlap exists for the ground-state reactants, the $^2P_{1/2}$ reactants are near-resonant with $\text{H}_2\text{O}^+ \tilde{A}$ -state bending vibrational levels with the largest Franck–Condon factors. Resonant charge-transfer reactions

^{a)}Geophysics Scholar.

^{b)}NRC postdoctoral fellow.

^{c)}PhotoMetrics, Inc., Woburn, MA 01801.

are thus expected to populate $\text{H}_2\text{O}^+ \tilde{A}$ -state vibrational levels that have significant Franck–Condon overlap, similar to the $\text{N}^+ + \text{H}_2\text{O}$ collision system. Unlike the N^+ reaction, which has several considerably exothermic reactive product ion channels, charge transfer is the only open channel for the $\text{Kr}^+ (^2P_{3/2}) + \text{H}_2\text{O}$ collision system. While endothermic for ground-state reactants, hydrogen atom abstraction



is exothermic by 0.3 eV for the excited spin–orbit state. The substantial spin–orbit splitting, as well as the significant difference in Franck–Condon overlap at resonance for the two spin–orbit states, suggests these states exhibit significantly different charge-transfer efficiencies. Such effects are well documented in $\text{Ar}^+ + \text{H}_2\text{O}$ charge-transfer collisions, where evidence of $\text{H}_2\text{O}^+ \tilde{A}$ -state population is only observed in the case of $\text{Ar}^+ (^2P_{3/2})$ reactants.⁶

In this work, we present guided-ion beam cross section and product ion TOF measurements, as well as low resolution luminescence spectra for the $\text{Kr}^+ + \text{H}_2\text{O}$ charge-transfer system over a wide range of collision energies. TOF spectra are modeled to yield low resolution product ion internal energy distributions as a function of collision energy. It will be shown that the observed charge-transfer luminescence is solely due to $\text{Kr}^+ (^2P_{1/2}) + \text{H}_2\text{O}$ reactants. The near-resonant $\text{H}_2\text{O}^+ \tilde{A}$ -state bending vibrational levels are less perturbed than those populated in the $\text{Ar}^+ + \text{H}_2\text{O}$ and $\text{N}_2^+ + \text{H}_2\text{O}$ collision systems⁶ and the presently reported luminescence spectra are therefore significantly less congested. Thus vibronic bands can be readily identified at modest spectral resolutions. The population of product ion vibrational states is estimated by modeling the low resolution optical spectra. A more detailed analysis of higher resolution luminescence spectra will be the subject of a subsequent publication.

Evidence of hydrogen-atom transfer chemiluminescence is also reported. Cross sections could not be determined for the chemical reaction channel since we are currently unable to distinguish between the various isotopes of Kr^+ and those of KrH^+ .

II. EXPERIMENTAL

Cross section and TOF measurements are conducted in an octopole guided-ion beam apparatus described previously in detail.⁹ Briefly, ions are produced in an electron impact ion source using 20 eV electrons and mass selected using a Wien velocity filter. The ion beam is then injected into the first of two rf octopole ion-beam guides, with a primary ion-beam resolution of 0.25 eV (FWHM). The first octopole guides the ions through a collision cell containing H_2O vapor at a pressure of approximately 0.15–0.2 mTorr. Primary and product ions exiting the collision cell enter the second octopole with equal rf phase but slightly lower dc-bias potential. The lower bias potential prevents the loss of slow product ions due to surface-potential barriers in the longer second octopole. From the exit end of the second octopole, primary and product ions are focused into a quadrupole mass filter, and following mass analysis, ions are detected using a channel electron multiplier.

The energy dependence of the reaction cross section was determined by scanning the octopole dc-bias potentials while measuring primary and product ion peak intensities. The quadrupole mass filter is operated at very low resolution so that the intensities of Kr isotopes contribute to a single primary flat-top band and H_2O^+ and secondary reaction H_3O^+ signals contribute to a single product band. Integral cross sections, σ , are obtained from the following expression:

$$\sigma = \frac{I_{\text{prod}}}{(I_{\text{prim}} + I_{\text{prod}})nl}, \quad (3)$$

where n is the neutral target gas density, l is the effective interaction length, I_{prim} is the transmitted primary ion beam current, and I_{prod} is the total product ion current.

The large difference in primary and secondary ion masses may cause mass discrimination effects. The primary ion-beam attenuation upon water vapor introduction into the collision cell is therefore also measured, in analogy to flow-tube rate constant measurement techniques.¹⁶ The attenuated intensity is compared to the intensity observed when water is introduced directly into the vacuum chamber of the octopole assembly to generate the same background pressure as observed during normal operation. No discrimination effect could be determined using this methodology. It is also found that attenuation measurements accurately reproduce $\text{O}^+ + \text{H}_2\text{O}$ charge-transfer cross sections, where no mass discrimination effects are expected and where no chemically reactive channels are observed. The absolute error of the cross-section measurements is estimated at $\sim 30\%$. The relative error is considerably smaller.

Product ion TOF spectra are recorded by generating 3–7 μs wide ion-beam pulses using a deflector electrode in the injection lens and then measuring the flight time of product ions relative to that of the primary ions. The primary ion laboratory energy is calibrated by comparing flight times at different second octopole potentials, and it is accurate to 0.05 eV. Background signal due to slow ions of previous TOF cycles is eliminated by temporarily switching off (bursting) the rf voltage following a TOF cycle, thus purging very slow ions that still reside in the ion guide.

The luminescence experiment was described in detail previously.⁶ It is conducted in the same tandem mass spectrometer system in which the guided-ion beam collision region is replaced with conventional ion optics and a collision cell. To improve sensitivity, a more intense dc plasma discharge source is used to generate the primary Kr^+ beam, and the H_2O vapor pressure in the collision cell is raised to ~ 1 mTorr. The ion source anode potential with respect to the filament is 50 V. Metastable Kr^+ ions are thus present in the beam. In situations where metastables affected the measurements, lowering the anode potential to 30 V eliminated the interference. The collision cell has highly reflective inner surfaces and is connected to a fiber optic bundle. Optical emissions produced in the chamber and entering the fibers are guided to a 0.156 m (F/3.7) Czerny Turner spectrograph positioned outside the vacuum chamber. The spectrograph is equipped with a Princeton Instruments liquid nitrogen cooled CCD area array detector.

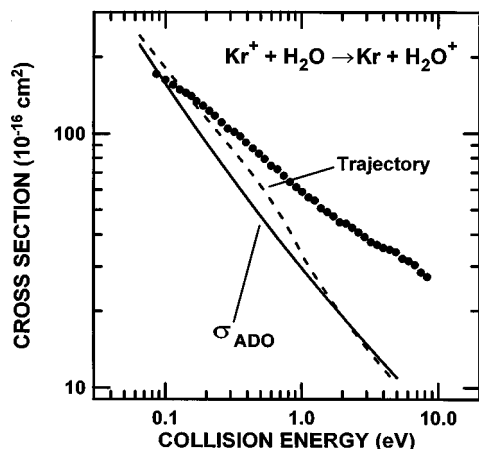


FIG. 1. Center-of-mass collision energy dependence of the $\text{Kr}^+ + \text{H}_2\text{O}$ charge-transfer cross section. The cross sections are compared to the capture cross section as determined by the average dipole orientation model (Refs. 19–21) and trajectory calculations parametrized by Su (Ref. 22).

Spectra are recorded by signal averaging between 2 and 15 h. Because an unintensified CCD array is used, significant numbers of cosmic ray “spikes” need to be removed from the raw data. Frequent readings are necessary in order to ensure correct identification of the cosmic ray induced signals. The unintensified array was chosen because of its high quantum efficiency ($\sim 40\%$) between 600 and 800 nm, the wavelength range of interest. The wavelength scale is calibrated using a mercury lamp, and a cubic polynomial function is fit to the calibration lines. The 4 nm FWHM resolution spectra have a wavelength scale that is accurate to within 1 nm. The spectral response of the detector was determined using a halogen tungsten lamp with a color temperature of 3200 K. Spectra are simulated using the methodology described in an earlier publication.⁶

III. RESULTS

A. Guided-ion beam measurements

The measured center-of-mass collision energy dependence of the $\text{Kr}^+ + \text{H}_2\text{O}$ charge-transfer reaction cross section is shown in Fig. 1 on a logarithmic scale. A least squares power law fit of the data in the range 0.2 to 1.0 eV shows that the cross section has an $E_T^{-0.47 \pm 0.01}$ dependence. For orientational purposes, the experimental data is compared to predictions of the average-dipole-orientation (ADO) model^{17–21} and a parametrized model empirically fitted to trajectory calculations by Su,²² both of which provide the energy dependence of the capture cross section of dipolar molecules. At collision energies below 0.2 eV, the measured cross sections agree with the capture model predictions, as do those of the $\text{N}^+ + \text{H}_2\text{O}$ and $\text{O}^+ + \text{H}_2\text{O}$ charge-transfer systems.^{7,10} At higher energies, the experimental cross sections are larger, as expected for the case where a direct mechanism is predominant. Unlike the $\text{N}^+ + \text{H}_2\text{O}$ and $\text{O}^+ + \text{H}_2\text{O}$ charge-transfer systems,^{7,10} the cross section decreases substantially with energy above 1 eV, resulting in a relatively small direct cross section.

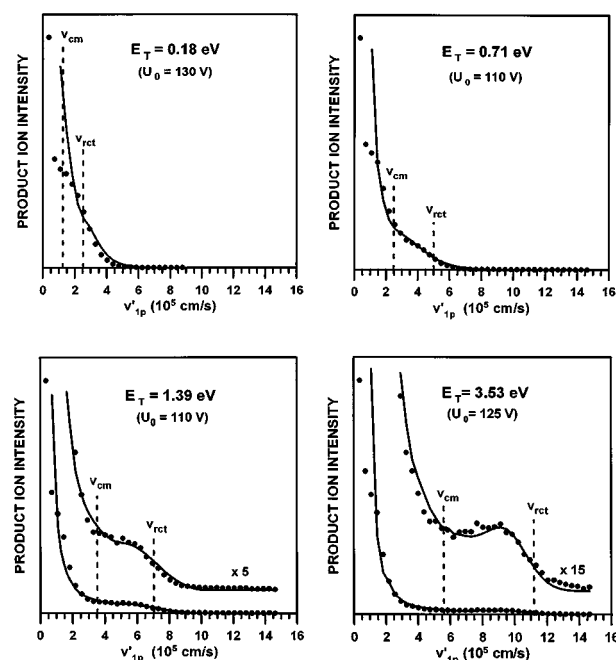


FIG. 2. Velocity-transformed time-of-flight distributions of the $\text{Kr}^+ + \text{H}_2\text{O}$ charge-transfer product ions at various collision energies. $v_{\text{c.m.}}$ and v_{rct} are the center-of-mass velocities and resonant charge-transfer forward-scattered velocities, respectively, for a target gas at rest. U_0 is the rf amplitude of the second octopole. The solid lines are numerical simulations as described in the text. The parameters providing the best fits are shown in Table I.

The charge-transfer mechanism and associated energy partitioning are investigated by recording product ion TOF spectra at collision energies ranging between 0.18 and 3.53 eV (c.m.). The raw TOF spectra are inverted to product-ion velocity distributions, $f(v'_{ip})$, where v'_{ip} represents the laboratory-frame product-ion velocity component parallel to the octopole axis. The TOF conversion and analysis procedure has been discussed previously.^{8,23} Examples of velocity-transformed spectra are shown in Fig. 2. The center-of-mass velocity, $v_{\text{c.m.}}$, and the velocity of resonantly forward-scattered product ions, v_{rct} , are indicated for each measurement. Both velocities have been determined for a target molecule at rest. Note that ions scattered into the direction of the primary ions are referred to as forward-scattered ions.

The TOF spectra shown in Fig. 2 were recorded with octopole rf amplitudes, U_0 , between 100 and 130 V, thus ensuring collection of all transverse velocity components. The distribution of transverse velocity components can in principle be determined by measuring TOF spectra at several rf amplitudes provided the octopole guiding potential has been calibrated with respect to transverse energy confinement.^{10,24} The difference of spectra recorded at different rf amplitudes then represent doubly differential cross sections with respect to parallel and transverse velocity components, thus yielding angular scattering distributions. The generation of difference spectra requires the measurement of absolute product ion yields at the respective TOF conditions. The large primary ion mass compared to that of the product ions in the present collision system, however, prevented such measurements because the primary ion confinement given by

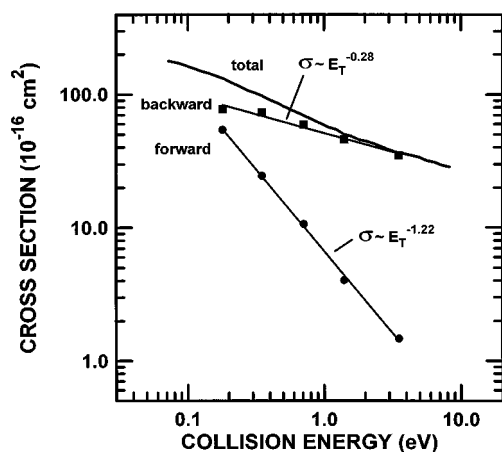


FIG. 3. Center-of-mass collision-energy dependence of the center-of-mass forward-scattered cross section including a comparison with the total and backscattered charge-transfer cross section. The forward-scattered cross section is determined from the TOF signal observed at velocities $v'_{1p} > v_{c.m.}$. The backscattered cross section consists of the difference between total and forward-scattered cross section.

the mass-dependent effective potential²⁴ is much weaker than that of the product ions. Consequently, significant primary ion beam losses occur at low rf amplitudes ($U_0 < 40$ V) between the first and second octopole, which have about a 10% difference in rf amplitude as a result of the capacitive coupling circuit used. As shown below, failure to measure transverse energy distributions does not grossly affect the analysis because the charge-transfer product angular distributions are adequately described by an osculating complex model.^{25,26}

A main band of products with near-zero laboratory-frame velocities is observed at all collision energies in Fig. 2. The predominance of near-thermal product ions is consistent with the large charge-transfer cross sections that are associated with long-range processes in which little momentum is transferred. A weaker band of forward-scattered product ions is observed, the intensity of which is strongly energy dependent. From the TOF measurements, a cross section for the center-of-mass forward-scattered ions is obtained by multiplying the fraction of product ion signal at velocities $v'_{1p} > v_{c.m.}$ by the total cross section obtained in the pulsed mode. (The pulsed cross section is lower than that obtained in a continuous mode because charge-transfer product ions with very small axial velocity components are purged from the octopole by temporarily switching off the rf power before initiating the next TOF cycle.) The energy dependence of the forward-scattered cross section is shown in Fig. 3 and is compared with the total charge-transfer cross section as well as the center-of-mass backscattered cross section. The latter is simply the difference between total and forward-scattered cross sections. A nonlinear least-squares fit of a E_T^n power-law yields $n = -1.22 \pm 0.06$ for the forward-scattered cross section, while $n = -0.28 \pm 0.06$ describes the backscattered cross section. The slope of the backscattered cross section agrees with the slope of the total cross section at high energies.

The marked decline of the forward-scattered cross section with energy implies that these ions are produced in large

impact parameter orbiting collisions, rather than small impact parameter head-on type collisions. Forward-scattered cross sections with an energy dependence of $\sim 1/E_T$ are observed in the other ion- H_2O charge-transfer systems investigated in this laboratory.^{7,9,10} The $1/E_T$ dependence is associated with the importance of the long-range ion-permanent dipole interaction in forming longer-lived intermediates. A pure ion-dipole interaction would result in a $1/E_T$ dependence of the capture cross section. Both the absolute magnitude and the energy dependence of the forward-scattered cross sections compare very closely to those observed in the $\text{N}^+ + \text{H}_2\text{O}$ system.¹⁰

Product ion internal energy distributions are obtained by simulating the velocity distributions in Fig. 2 using the osculating complex model^{25,26} and the methodology described by Gerlich.²³ The osculating complex model assumes that product angular distributions are the result of an intermediate complex with an exponential distribution of decay times. The experimental data is fit to calculated intensity distributions according to

$$I(v'_{1p}) = \sum_i c_i S_i[v'_{1p}; \Delta E_T(i), \tau_r/\tau_c(i)], \quad (4)$$

where $S_i[v'_{1p}; \Delta E_T(i), \tau_r/\tau_c(i)]$ are calculated velocity distributions for a given complex lifetime and translational energy transfer, and are normalized with respect to the integrated intensity; ΔE_T is the translational energy transfer; τ_r/τ_c is the complex rotational period-to-lifetime ratio; and c_i are the coefficients obtained from a least-squares fitting procedure using a singular-value-decomposition algorithm.²⁷ The use of the osculating complex model is validated by modeling TOF spectra recorded at both high and low rf amplitudes and verifying that the same ΔE_T distributions reproduce both measurements. For all of the collision energies investigated in Fig. 2, a second spectrum has been recorded with an rf amplitude of 20 V. Calibration of the octopole confinement shows that an amplitude of 20 V effectively confines those ions with transverse translational energies below 150 meV. A comparison of a pair of spectra taken at high and low rf amplitudes at $E_T = 1.4$ eV is shown in Fig. 4. The solid lines in Fig. 2 and 4 are simulated velocity distributions according to Eq. (4). For the low rf amplitude conditions, the intensity of those product ions for which the transverse energy is greater than 150 meV is set to zero in the simulations. The fact that the optimal fit parameters yield good reproduction of the experimental data recorded at both high and low rf amplitudes, as shown in Fig. 4, confirms that the osculating complex model describes the angular distributions of the present experiments.

The fit between the calculated curves and the experimental data is not optimal at low velocities. This is attributed to octopole rod surface potential inhomogeneities that mostly affect the flight time of slow ions. In the low rf amplitude measurement in Fig. 4, some very fast ions are also noticeable that are not reproduced in the simulation. The rf-amplitude dependence of this signal shows that these ions can be attributed to charge-transfer products formed by primary ions with relatively large transverse velocity compo-

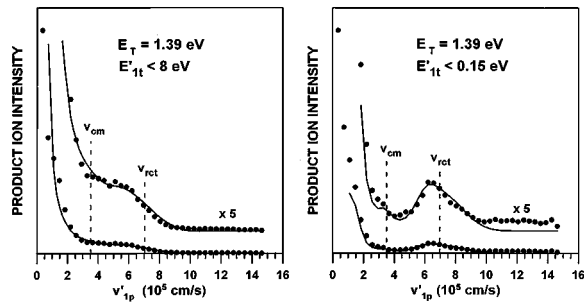


FIG. 4. Second octopole rf-amplitude dependence of charge-transfer product ion TOF spectra at $E_T = 1.39$ eV. The spectrum to the left is obtained at an amplitude of 110 V, corresponding to a maximum transverse energy confinement of 8 eV for H_2O^+ . The spectrum to the right is obtained at an rf amplitude of 20 V, corresponding to a maximum confinement of 0.15 eV. The solid lines represent numerical simulations including the different transverse confinement conditions. The same distribution of translational energy transfer is used to fit both spectra, confirming the validity of the oscillating complex model.

nents that may have experienced heating in a first reflection off the effective potential of the octopole and that were not properly discriminated against because of an insufficient number of additional reflections due to the short length of the first octopole. This inefficient rejection of “bad” trajectories is associated with the high primary ion mass since such an effect has not been observed with other lighter primary ions. The problem could be eliminated by lowering the rf frequency. This, however, would affect the stability of the H_2O^+ trajectories. The signal of very fast ions is only a small fraction of the total forward-scattered signal, and therefore does not affect the analysis of the data.

The parameters yielding the best fits are shown in Table I and graphically illustrated in Fig. 5. The table includes the adjustable variables of the model, i.e., the translational exoergicity and the complex rotational period to lifetime ratio. Note that negative values of ΔE_T signify translational energy transferred into internal energy. The resulting internal energy distributions have been corrected for slow ions that are not accounted for when using the rf burst technique. Those ions are attributed to resonant large impact parameter ($\tau_r/\tau_c > 10$) events. Table I also includes the cross sections, $\sigma(\tau_r/\tau_c, \Delta E_T)$, associated with a particular complex lifetime and energy transfer.

All of the experimental velocity distributions are adequately fit using two complex lifetimes: one representing a direct charge-transfer mechanism ($\tau_r/\tau_c \geq 15$), and another representing the formation of longer-lived complexes ($\tau_r/\tau_c \leq 4$). The main band in the TOF spectra is attributed to collisions where the complex lifetime is significantly shorter than the rotational period. The forward-scattered bands in the TOF spectra are primarily due to orbiting collisions with smaller τ_r/τ_c , which are presumably associated with smaller impact parameters. Except at the lowest collision energy investigated, the ratio, τ_r/τ_c , that reproduces the forward-scattered fall-off function most accurately is approximately 4 ± 1 .

At all collision energies, the direct charge-transfer component exhibits no noticeable translational-to-internal energy

TABLE I. Simulation parameters for $\text{Kr}^+ + \text{H}_2\text{O}$ charge-transfer TOF spectra. E_T is the collision energy; c represents the statistical weight of the calculated velocity distribution, $S_i[v'_{1p}; \Delta E_T, \tau_r/\tau_c]$; ΔE_T is the translational exoergicity; and τ_r/τ_c is the complex rotational period-to-lifetime ratio. Energy transfer cross sections, $\sigma(\tau_r/\tau_c, \Delta E_T)$, are given by $c \cdot \sigma_0(E_T)$, where $\sigma_0(E_T)$ is the respective integral charge-transfer cross section.

E_T (eV)	τ_r/τ_c	c	ΔE_T (eV)	$\sigma(\tau_r/\tau_c, \Delta E_T)$ (10^{-16} cm ²)
0.18	15	0.308	0.0	40.5
	1	0.066	−0.2	8.7
	1	0.172	−0.1	22.6
	1	0.120	0.0	15.8
	1	0.074	0.1	9.7
	1	0.088	0.2	11.6
	1	0.072	0.3	9.5
	1	0.038	0.4	5.0
	1	0.033	0.5	4.3
	1	0.029	0.6	3.8
	0.71	15	0.893	62.1
	4	0.003	−0.8	0.2
	4	0.016	−0.6	1.1
	4	0.031	−0.4	2.2
	4	0.017	−0.2	1.2
1.39	4	0.004	0.0	0.3
	4	0.003	0.2	0.2
	4	0.008	0.4	0.6
	4	0.010	0.6	0.7
	4	0.016	0.8	1.1
	15	0.887	0.0	44.9
	4	0.006	−1.4	0.3
	4	0.007	−1.0	0.4
	4	0.034	−0.6	1.7
	4	0.016	−0.2	0.8
	4	0.009	0.2	0.5
	4	0.017	0.6	0.9
	4	0.013	1.0	0.7
	4	0.010	1.4	0.5
	3.53	30	0.716	26.1
3.53	4	0.010	−2.5	0.4
	4	0.044	−2.0	1.6
	4	0.064	−1.5	2.3
	4	0.071	−1.0	2.6
	4	0.055	−0.5	2.0
	4	0.021	0.0	0.8
	4	0.020	0.5	0.7

transfer, implying that the majority of product ions are formed with internal energy corresponding to the charge-transfer exothermicity or less (positive translational energy transfer resulting in laboratory backscattered ions cannot be identified as such in the present TOF technique). In contrast, energy transfer is significantly more efficient in those collisions proceeding via a longer-lived intermediate. Both negative and positive translational energy transfer are evident.

C. Luminescence measurements

Low resolution (4 nm, FWHM) luminescence spectra, taken at collision energies between 0.1–15 eV (c.m.), are shown in Fig. 6. The measurements were taken with a 300 groove/mm, 1000 nm blaze grating. The spectra consist of a structured broad band that are attributed to $\text{H}_2\text{O}^+ \tilde{A}^2A_1 - \tilde{X}^2B_1$ emissions along with several Kr atomic emissions. The 50 V anode to filament potential difference of

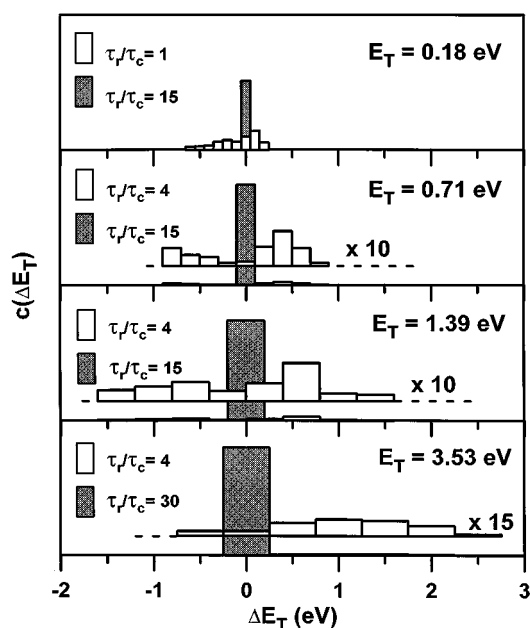


FIG. 5. Schematic representation of the simulation parameters yielding the best fits of the TOF spectra shown in Fig. 3 and listed in Table I.

the dc discharge source is sufficient to produce metastable ions, and the atomic emissions can thus be attributed to small amounts of metastable ions in the beam. The dashed lines in the figure indicate the “resonant wavelengths,” λ_R , for the $^2P_{3/2}$ and the $^2P_{1/2}$ spin-orbit states of Kr^+ . The resonant

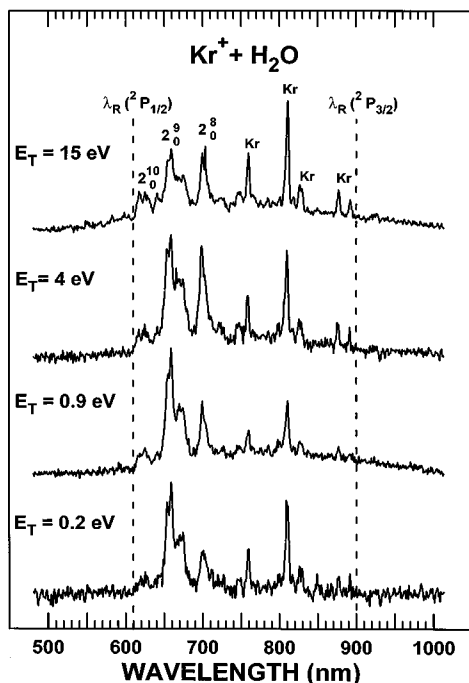


FIG. 6. Low resolution luminescence spectra (4 nm FWHM) recorded at various center-of-mass collision energies. The dashed lines indicate the emission wavelength corresponding to a transition between a resonant level and the product ground rovibronic state for the respective spin-orbit states of the reactant ion. At all collision energies, atomic Kr lines are also observed that are attributed to metastables in the Kr^+ beam.

wavelengths correspond to an energy, hc/λ_R , equal to the respective spin-orbit charge-transfer exothermicities [Eq. (1)] and thus represent the shortest wavelengths at which emissions are observed following the population of a resonant level. For $\text{Kr}^+(^2P_{3/2}) + \text{H}_2\text{O}$ reactants, the resonant wavelength is 898 nm, while it is 608 nm for $\text{Kr}^+(^2P_{1/2}) + \text{H}_2\text{O}$.

The spectroscopy and structure of H_2O^+ has been discussed previously in detail.^{28–30} Briefly, H_2O^+ has a doubly degenerate $^2\Pi_u$ ground state in the linear conformation. The degeneracy is lifted upon bending the molecule, yielding two nondegenerate components, 2A_1 and 2B_1 . The \tilde{X}^2B_1 lower component has a bent equilibrium conformation and the \tilde{A}^2A_1 upper component is linear. Consequently, Franck-Condon transitions from the H_2O ground vibronic state to the $\text{H}_2\text{O}^+ \tilde{A}$ state produce predominantly bending vibrational excitation.

Recently, Brommer *et al.*³⁰ have performed *ab initio* calculations taking Renner-Teller and spin coupling into account and determine a barrier to linearity of 7886 cm^{-1} which is 1301 cm^{-1} lower than that obtained by Jungen *et al.*²⁹ when fitting the experimental data^{14,28} with respect to the experimental bending vibrational assignment. Since 1301 cm^{-1} corresponds to two \tilde{A} -state bending vibrational quanta of the linear molecule, Brommer *et al.* conclude that the experimental work overlooked the two lowest bending vibrational levels. As shown in a separate communication,³¹ the simulations of the present low-resolution data can only reproduce the experiment if the vibronic transition moments calculated by Jungen *et al.*²⁹ are reassigned according to the *ab initio* calculations, thus verifying the new assignment.

The assignments of $\text{H}_2\text{O}^+ \tilde{A} - \tilde{X}$ bands in Fig. 6 refer to $(0, v'_2, 0) \rightarrow (0, v''_2, 0)$ transitions, where v'_2 are vibrational quantum numbers of the \tilde{A} -state bending mode of the linear molecule, v'_2 , as assigned by Brommer *et al.*³⁰ Coarse assignment of vibronic bands is already possible at the low resolution of 4 nm FWHM, which was not the case in our previous luminescence work. Contrary to the ion- H_2O systems studied previously in this laboratory,⁶ the transition moments for $(0, v'_2, 0) \rightarrow (0, v''_2 > 0, 0)$ transitions are considerably weaker than for $(0, v'_2, 0) \rightarrow (0, 0, 0)$ transitions, thus providing for less congested spectra.

For $\text{Kr}^+(^2P_{1/2})$ primary ions, the reactant energy is almost exactly resonant with $\text{Kr} + \text{H}_2\text{O}^+ \tilde{A}^2A_1(0, 10, 0)$ products. It can be readily deduced from the spectra that the $v'_2 = 10$ level is the highest \tilde{A} -state bending vibrational level with significant population and that primarily levels at and below resonance are populated. Weak luminescence at shorter wavelengths than resonance is only discernable at $E_T = 0.9 \text{ eV}$ and higher if a spectrograph grating with 400 nm blaze is chosen.

In the case of resonant charge transfer involving the $\text{Kr}^+(^2P_{3/2})$ reactant (a statistical ratio of spin-orbit states is expected in the ion beam), one would expect to observe luminescence signals at and above $\sim 900 \text{ nm}$. Except for a very weak band observed at 940 nm in the $E_T = 15 \text{ eV}$ spectrum, little-to-no signal is observed at those wavelengths. The weak band is attributed to the third harmonic of OH $A^2\Sigma - X^2\Pi$ emissions with (0–0) bandhead at 306.4 nm.

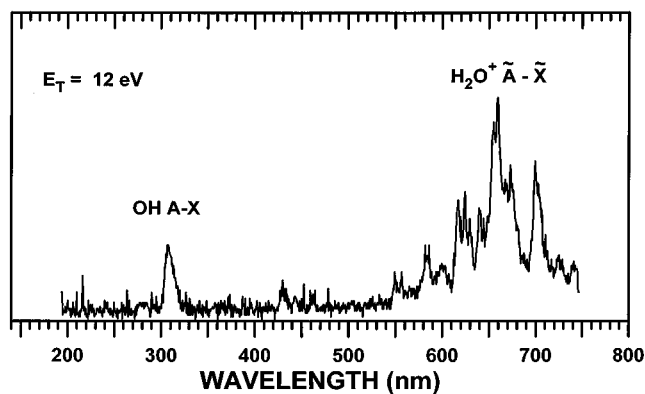


FIG. 7. Low resolution spectrum depicting evidence of OH A–X emissions. The weak bands at ~ 430 nm are not identified.

This is verified by recording a significantly blueshifted spectral range. A spectrum obtained with a 300 groove/mm, 300 nm blaze grating at a collision energy of 12 eV is shown in Fig. 7. The source of the OH emissions and the weak band at 430 nm is discussed below.

The association of the weak band at 940 nm with OH A–X emissions leads to the conclusion that no evidence of near-resonant $\text{Kr}^+(^2P_{3/2}) + \text{H}_2\text{O}$ charge-transfer products is present in the observed $\text{H}_2\text{O}^+\tilde{\text{A}}-\tilde{\text{X}}$ spectrum. This indicates that either the experiment is not sensitive to detection of these product ions or that spin–orbit selectivity exists for this charge-transfer reaction. The transition moment of the $\tilde{\text{A}}(0,5,0)-\tilde{\text{X}}(0,0,0)$ transition expected near 900 nm is very small compared to the transitions associated with $\text{Kr}^+(^2P_{1/2})$ reactants. From the transition moments, the noise level at 900 nm and above and the respective spectral sensitivity, we determine an upper limit for the population of the $\tilde{\text{A}}(0,5,0)$ vibronic state that is comparable to that determined for the $\tilde{\text{A}}(0,10,0)$ level, the nearest-resonant level of $\text{Kr}^+(^2P_{1/2}) + \text{H}_2\text{O}$ reactants. Evidence regarding spin–orbit selectivity based on the optical work is thus inconclusive.

The low-resolution spectra of Fig. 6 have been simulated using the methodology described in Ref. 6 which is only briefly described here. The H_2O^+ vibronic state populations are determined from the vibronic band intensities using the following expression for the rotational line intensities in energy units per second:

$$I(N' \rightarrow N'') \sim n(\nu'_2, K'_a) \nu'^4 |\langle \phi(\nu'_2, K'_a) | \mu | \phi(\nu''_2, K''_a) \rangle|^2 \times S(N' \rightarrow N''), \quad (5)$$

where $n(\nu'_2, K'_a)$ is the number density populating the excited level $|\nu'_2, K'_a\rangle$; K_a is the asymmetric rotor rotational quantum number with respect to the A axis; ν is the line frequency; $|\langle \phi(\nu'_2, K'_a) | \mu | \phi(\nu''_2, K''_a) \rangle|$ is the respective transition moment, and $S(N' \rightarrow N'')$ are intensity factors including the nuclear statistics, the rotational partition function, and a Boltzmann factor. K_a becomes the vibronic angular momentum quantum number, K , in the linear molecule, for which the A rotational constant is infinitely large.

The spectroscopic term values and rotational constants of the relevant $\text{H}_2\text{O}^+\tilde{\text{A}}$ -state levels are listed in Table II. The

TABLE II. $\text{H}_2\text{O}^+\tilde{\text{A}}$ -state spectroscopic constants used for simulations. The constants are those published by Lew (Ref. 27) except for the $\nu'_2 = 8$, $K'_a = 3$ values where T_0 are the calculated values of Brommer *et al.* (Ref. 16) and B_{eff} are those calculated by Jungen *et al.* (Ref. 28). Except for energy gaps, ΔE , between $\text{Kr}^+(^2P_{1/2})$ reactants and respective products, which are given in eV, all values are listed in wave numbers. Two B_{eff} values are given for cases of high asymmetry ($K'_a = 1$).

ν'_2	$K'_a = 0$	$K'_a = 1$	$K'_a = 2$	$K'_a = 3$
8	T_0	14 329		14 207
	ΔE	–0.263		–0.278
	B_{eff}	9.26 8.51		9.643
9	T_0	15 302.45	15 225	
	ΔE	–0.143	–0.152	
	B_{eff}	8.94	8.90	
	D_0	0.002		
10	T_0	16 253		16 098
	ΔE	–0.025		–0.044
	B_{eff}	9.45 8.36		9.13
11	T_0	17 263.10	17 175	
	ΔE	0.100	0.090	
	B_{eff}	8.78	8.83	
	D_0	–0.006		
12	T_0	18 234		18 065
	ΔE	0.221		0.200
	B_{eff}	9.54 8.38		9.23

asymptotic energy gaps with respect to $\text{Kr}^+(^2P_{1/2}) + \text{H}_2\text{O}$ reactants are also listed. When available, the constants were obtained from the experimental work of Lew.²⁸ The remaining values were obtained from the calculations of Jungen *et al.*²⁹ and Brommer *et al.*³⁰ The vibronic transition moments used in the simulations are those calculated by Jungen,²⁹ and reassigned according to the calculations of Brommer *et al.*³⁰ The simulations assume thermal rotational populations as expected in large-impact parameter grazing collisions. The only variable is thus $n(\nu'_2, K'_a)$. Only product states with $K'_a < 4$ are considered.

The simulation results are tabulated in Table III, and the derived approximate $\text{H}_2\text{O}^+\tilde{\text{A}}$ -state vibrational populations

TABLE III. Distributions, $n(\nu'_2, K'_a)$, derived from simulating $\text{Kr}^+ + \text{H}_2\text{O}$ charge-transfer luminescence spectra. Except for the rotation about the A axis, a rotational temperature of 300 K is assumed. The population of only two K'_a sublevels per vibrational level is considered. No evidence of emissions could be identified for $\nu'_2 > 12$ and $\nu'_2 < 8$.

ν'_2	K'_a	$E_T = 0.2$ eV	$E_T = 0.9$ eV	$E_T = 4.0$ eV	$E_T = 15$ eV
8	Total	0.27	0.30	0.38	0.33
	1	0.17	0.18	0.26	0.18
	3	0.10	0.12	0.12	0.15
9	Total	0.60	0.53	0.45	0.33
	0	0.30	0.26	0.20	0.15
	2	0.30	0.27	0.25	0.18
10	Total	0.13	0.11	0.11	0.15
	1	0.04	0.03	0.03	0.06
	3	0.09	0.08	0.08	0.09
11	Total	0	0.035	0.035	0.06
	0	0	0.020	0.013	0.03
	2	0	0.015	0.022	0.03
12	Total	0	0.02	0.022	0.12
	1	0	0.01	0.011	0.05
	3	0	0.01	0.011	0.07

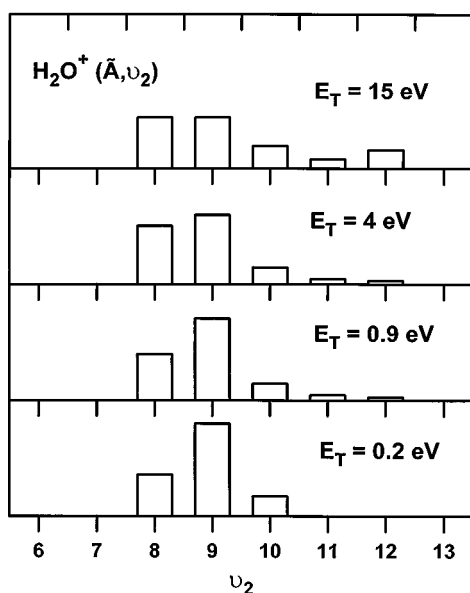


FIG. 8. Schematic representation of H_2O^+ \tilde{A} -state vibrational populations as a function of collision energy determined from low-resolution luminescence measurements.

are illustrated in Fig. 8. The populations of the $v'_2 = 11$ and 12 states are determined from the spectral range shown in Fig. 7 using the 300 nm blaze grating. As seen in Fig. 7, the respective emissions below 600 nm become significantly more pronounced when using the uv blaze. Emissions from levels higher than $v'_2 = 12$ could not be identified.

It is important to note that the presented populations are subject to considerable error due to the low resolution of the experiments. A rotational and K -sublevel analysis is necessary to derive more accurate populations. The K -sublevel structure is only partially resolved at the present resolution. First inspection of higher-resolution measurements, for example, reveal major discrepancies between calculated and measured $(0,9,0)-(0,0,0)$ bands if a thermal rotational and K distribution is assumed. This may be an indication of high K -level population in the $v'_2 = 10$ state, as well as of hyperthermal rotational populations. High K levels were identified in near resonant vibrational states of Ar^+ and $\text{N}_2^+ + \text{H}_2\text{O}$ charge-transfer products⁶ that interfered with the bands of the next lower vibrational level. If this were the case in the present system, the derived populations shown in Fig. 8 would need considerable revision. A more detailed analysis of angular momentum effects in the $\text{Kr}^+ + \text{H}_2\text{O}$ collision system will be presented in a subsequent publication of higher resolution (0.8 nm FWHM) luminescence studies. The analysis of the present low-resolution spectra, nevertheless, demonstrates how the vibrational product distributions are affected by translational energy. The H_2O^+ vibrational populations are observed to broaden as the translational energy is increased. Interestingly, the K -sublevel populations indicate a population reversal for the $v'_2 = 10$ state, the nearest resonant level. This further indicates the possibility of higher angular momentum states.

The OH $A-X$ emissions shown in Fig. 7 could be due to a collisional dissociation channel or due to the hydrogen

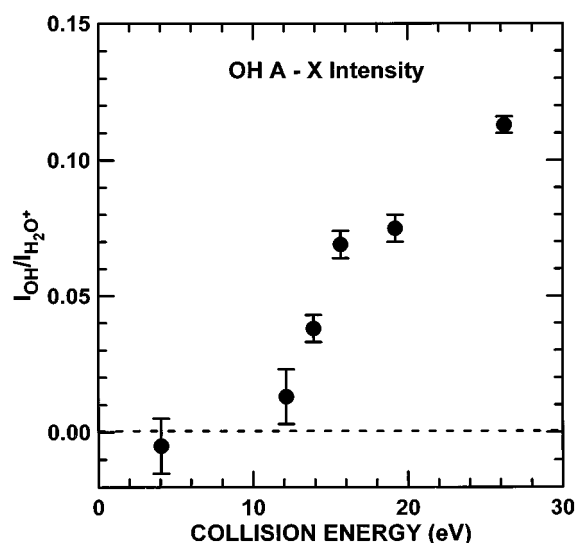


FIG. 9. Energy dependence of the OH $A-X$ signal relative to the H_2O^+ $\tilde{A}-\tilde{X}$ intensity.

atom transfer reaction [Eq. (2)]. Spectra such as the one shown in Fig. 7 were recorded over a wide range of energies to determine the onset of $A-X$ emissions. In the process, it was determined that metastable ions can contribute substantially to the OH signal, since they are observed below the thermodynamic threshold of 3.7 eV for $\text{Kr}^+ (^2P_{1/2}) + \text{H}_2\text{O}$ reactants. This signal disappears, however, if the anode voltage of the dc discharge ion source is reduced from 50 to 30 V. The bands at 430 nm seen in Fig. 7 also vanish and are, therefore, attributed to some metastable process that is not further investigated here. The relative OH $A-X$ signal obtained at an anode voltage of 30 V is plotted in Fig. 9 as a function of collision energy. The normalized intensity is the ratio between the OH signal and the total H_2O^+ signal, which may be considered relatively constant with collision energy at these high energies. An OH $A-X$ onset of ~ 11 eV is observed. This onset is almost identical to that reported for $\text{Ar}^+ + \text{H}_2\text{O}$ atom-transfer chemiluminescence,³² where the endothermicity for OH $A \ ^2\Sigma$ production is 3.1 eV. In that work, the onset was compared to the onset for the situation where energy transfer is governed by a spectator-stripping type mechanism.^{33–36} The spectator-stripping translational-to-internal energy transfer increases linearly with collision energy and is given by the pairwise energy³⁷

$$E_{\text{pair}} = (1 - m_1/m'_1)E_{\text{lab}}, \quad (6)$$

where m_1 is the primary ion mass, m'_1 is the product ion mass, and E_{lab} is the primary ion laboratory frame energy. Application of Eq. (6) leads to spectator-stripping OH A -state thresholds of 39 and 56 eV c.m. for the $\text{Ar}^+ + \text{H}_2\text{O}$ and $\text{Kr}^+ (^2P_{1/2}) + \text{H}_2\text{O}$ collision systems, respectively. The observed chemiluminescence onsets are considerably lower than those thresholds, but lie above the collision-induced dissociation onset of 9.2 eV c.m. In the $\text{Ar}^+ + \text{H}_2\text{O}$ case, the OH A rotational distributions are very similar to those observed in the $\text{N}_2^+ + \text{H}_2\text{O}$ atom transfer reaction, for which OH $A-X$ luminescence is observed below the collision-induced disso-

ciation threshold and thus cannot be attributed to collision-induced dissociation.³² It was, therefore, concluded that the OH emissions originated from atom-transfer reaction products. The similarities between the Kr^+ and Ar^+ systems suggest that the present OH $A-X$ emissions are also atom-transfer chemiluminescence. As mentioned in Sec. I, we cannot resolve KrH^+ from Kr^+ mass spectrometrically to further corroborate the existence of this channel. However, small amounts of KrH^+ have been observed in $\text{Kr}(\text{H}_2\text{O})^+$ photodissociation experiments, demonstrating that the activated collision complex can decay to chemical reaction products.³⁸

IV. DISCUSSION

The present charge-transfer cross sections measured for a spin-orbit mixture of $\text{Kr}^+(^2P_J) + \text{H}_2\text{O}$ reactants are comparable to, if not larger than, capture model predictions at energies below 1 eV, similar to the O^+ , N_2^+ , and $\text{N}^+ + \text{H}_2\text{O}$ charge-transfer systems.^{7,9,10} Capture models provide good predictions of total reaction cross sections if the dynamics involve statistical partitioning of the reaction energy. This is certainly not the case for charge-transfer reactions of small polyatomic systems. The comparison to capture models, therefore, only serves the purpose to assess the efficiency of charge transfer. The large low-energy cross sections imply that either both spin-orbit states have high charge-transfer probabilities, or one of the reactant states exhibits an exceptionally high long-range coupling. According to energy resonance and Franck-Condon arguments,^{1,2} $\text{Kr}^+(^2P_{3/2}) + \text{H}_2\text{O}$ reactants should exhibit a small charge-transfer cross section due to the unfavorable Franck-Condon factors near resonance, whereas a large charge-transfer cross section is expected for $\text{Kr}^+(^2P_{1/2})$ reactants, where resonant charge-transfer leads to $\text{H}_2\text{O}^+ \tilde{A}$ -state levels that have the largest Franck-Condon overlap with the respective reactants. These arguments successfully clarify observations in the $\text{Ar}^+ + \text{H}_2\text{O}$ system,⁶ where luminescence is only detected from H_2O^+ states near-resonant with the $\text{Ar}^+(P_{3/2}) + \text{H}_2\text{O}$ reactants. In that system, the Franck-Condon overlap for the excited spin-orbit reactants is vanishingly small. Since the optical studies of the present work are inconclusive regarding spin-orbit selectivity, reactant state-selected studies are necessary to resolve this issue.

As in the other ion- H_2O systems investigated in this laboratory, the TOF analysis (Fig. 5) demonstrates that we can differentiate between two types of trajectories: large-impact parameter near straight-line trajectories and smaller impact parameter orbiting trajectories. At the low collision energy of 0.18 eV (c.m.), 30% of charge-transfer ions are determined to be formed in long-range direct processes, a significant departure from pure capture collisions as assumed by the ADO and trajectory predictions. Whereas the near straight-line trajectories result in no measurable energy transfer, the orbiting collisions are well described by an osculating complex^{25,26} and exhibit broad distributions of energy transfer due to the deeper penetration of the intermolecular potential and the longer interaction times. At 3.53 eV, orbiting trajectories exhibit a strong preference for positive translational energy transfer. This can be related to the small cap-

ture radius at higher translational energies with the consequence that orbiting trajectories negotiate the repulsive part of the interaction potential where energy transfer is efficient.

The TOF studies are not informative regarding the product internal energy distributions resulting from the predominant long-range charge-transfer collisions. The luminescence measurements, on the other hand, allow a detailed analysis of $\text{H}_2\text{O}^+ \tilde{A}$ -state product vibrational distributions of the main long-range processes. Only pure bending vibrational transitions are observed, i.e., no evidence of stretch excitations is detected. This further agrees with Franck-Condon predictions, since the structure of the \tilde{A} -state band of the H_2O photoelectron spectrum¹³⁻¹⁵ is almost entirely attributable to bending vibrational states at the pertinent energies. At low collision energies, the determined distributions exhibit a preference for populating the two bending vibrational states below the nearest resonant (0,10,0) level ($\Delta E = -0.025$ eV) of $\text{Kr}^+(^2P_{1/2}) + \text{H}_2\text{O}$ reactants. A similar observation has been made in the product ion vibrational distributions of the Ar^+ and $\text{N}_2^+ + \text{H}_2\text{O}$ and the $\text{O}^+(^2P, ^2D) + \text{HCl}$ charge-transfer systems.^{6,39,40} In all of these systems, the reactant long-range interaction is significantly more attractive than that of the products due to the presence of a dipole. Within the framework of the Bauer-Fisher-Gilmore model for vibronic nonadiabatic transitions,⁴¹ we, therefore, have a manifold of reactant vibronic levels that dip into a manifold of product vibronic levels as the reactants approach, provided the dipole is oriented such as to generate an attractive interaction. The failure to observe significant population of endothermic levels is a clear indication that an attractive long-range potential is probed and that a favored direction of the neutral target dipole therefore exists. The strong long-range interaction causes the nearest resonant \tilde{A} -state product level (0,10,0) to experience crossings at very long range (6–10 Å), where the electronic coupling is still very weak, thus explaining the small respective charge-transfer probability.

The $\text{F}^+ + \text{CO}$ charge-system demonstrates that a preference of levels below resonance is not the general rule. In that system, the product-state distribution is almost symmetric with respect to the resonant $\text{F}(^2P) + \text{CO}^+(A \ ^2\Pi, v=5)$ level at collision energies below 20 eV.^{42,43} This could imply that the dipole orientation is not relevant for the $\text{F}^+ + \text{CO}$ charge-transfer system. The preference of below-resonant states in all of the ion- H_2O systems investigated so far may be due to a required overlap between the incident ion charge and the lone-pair orbitals of the H_2O oxygen atom. This would necessitate an attack from the attractive side of the dipole. Such a scenario would also explain the large $\text{O}^+ + \text{H}_2\text{O}$ charge-transfer cross section⁷ despite the extremely unfavorable Franck-Condon overlap at resonance. That system happens to be resonant where the H_2O^+ Renner-Teller states meet in a linear geometry. The large cross section can be rationalized through the population of the (2,0,0) ($\Delta E = 0.20$ eV) and (1,1,0) ($\Delta E = 0.41$ eV) vibrational levels of the \tilde{X} state that are readily observed in the photoelectron spectrum¹³⁻¹⁵ and thus have substantial Franck-Condon overlap.

A remarkable feature is the failure to detect products formed in $v'_2 = 7$ and lower states at all the collision ener-

gies investigated in this work. An analogous observation was made in the $\text{Ar}^+ + \text{N}_2^+ + \text{H}_2\text{O}$ charge-transfer systems and was attributed to a predominance of the hydrogen atom transfer channel at the smaller impact parameters that are necessary to access the off-resonant states. Because of the isotope and mass resolution issues mentioned earlier, it is not clear whether hydrogen atom transfer plays an important role in the $\text{Kr}^+ + \text{H}_2\text{O}$ system. Alternately, the failure to observe states below certain off-resonant energies may be attributed to the reactant potential well depth that limits how deep the product vibronic manifold can be penetrated, or to a predominantly adiabatic behavior at the shorter intermolecular distances at which these states are accessed.

At 0.2 eV, the $v'_2 = 9$ level is primarily populated. Despite the importance of longer-lived intermediates, as demonstrated by the TOF measurement, the distribution is distinctly nonstatistical, confirming that statistical models such as phase space theory^{44–46} do not apply to nonadiabatic reaction systems. As the collision energy is increased, the product vibrational distribution broadens noticeably. Luminescence from the $v'_2 = 7$ level can also be identified at collision energies above 100 eV using higher resolution, as will be presented in a future publication. Collision-energy induced broadening of charge-transfer product vibrational distributions has previously been observed in the ion+HCl^{39,40} and $\text{F}^+ + \text{CO}$ systems.⁴³ The broadening is best explained using the concept of the dynamic energy range, δE , introduced by Gislason and co-workers.^{1,2,47} The dynamic energy range is directly related to the energy uncertainty associated with a characteristic collision time, and thus

$$\delta E \sim g, \quad (7)$$

where g is the relative velocity. The semiclassical models by Gislason and co-workers predict that with increasing collision energy, δE eventually covers the entire energy range of states populated in a Franck–Condon transition, and a Franck–Condon distribution of the product states is then expected. This has indeed been observed in the $\text{Ar}^+ + \text{N}_2^+ + \text{H}_2\text{O}$ charge-transfer systems at near keV collision energies.⁶

The similar endoergic energy-transfer cross sections in relationship to near-resonant charge-transfer observed in the TOF studies (Table I) and in the luminescence studies at low collision energies (<10 eV) imply that the endothermic levels observed in the luminescence studies are the result of longer-lived intermediates. At 15 eV, the population of endothermic levels is clearly higher than what can be associated with orbiting collisions in the TOF study. Off-resonant long-range contributions rendered more probable due to the higher dynamic range at higher collision energies may thus account for the significant endothermic state-to-state cross sections. A discrepancy exists between the TOF and luminescence studies in that the TOF studies of orbiting collisions indicate the population of bending vibrational levels significantly higher than the $v'_2 = 12$ level at 1.39 and 3.53 eV. Those collisions leading to higher excited vibronic products are associated with smaller impact parameter collisions that experience significant energy transfer on the repulsive part of the interaction potential. A conceivable explanation for the

failure to observe the endothermic product states is that the strong short-range interaction induces a radiationless transition from \tilde{A} -state products to the \tilde{X} state. Alternately, high rotational excitation may broaden the low-resolution bands of the respective endothermic levels, thereby reducing their intensity. This issue will be further pursued in the analysis of higher-resolution luminescence studies including a rotational and K -sublevel analysis. The present work only includes the lowest two K levels ($K=0,2$ for odd states, $K=1,3$ for even states) of a vibrational state. The low-resolution spectra hint at K -state distributions of the nearest resonant levels that do not reflect Franck–Condon transition probabilities from thermal H_2O (Table III). These anomalous K -state distributions, which have already been observed in the $\text{Ar}^+ + \text{N}_2^+ + \text{H}_2\text{O}$ charge-transfer systems,⁹ may provide important clues regarding the coordinate-specific details of the charge-transfer dynamics.

V. CONCLUSION

The $\text{Kr}^+ (^2P_{3/2}, ^2P_{1/2}) + \text{H}_2\text{O}$ charge-transfer cross section is measured in the collision energy range of 0.05 and 10 eV (c.m.). TOF studies of H_2O^+ products enable the distinction between forward and backscattered ions. The $E_T^{-1.22}$ dependence of the cross section for producing forward-scattered ions signifies that they primarily originate from orbiting collisions associated with smaller impact parameters. The TOF analysis invoking the osculating complex model^{25,26} demonstrates that significant energy transfer is associated with the forward-scattered products. The average complex lifetime of the orbiting collisions is less than a rotational period at energies above 0.7 eV. The backscattered cross section exhibits an $E_T^{-0.28}$ dependence and at energies above 1 eV is mainly attributed to a long-range direct charge-transfer mechanism involving near straight-line trajectories. Luminescence measurements of $\text{H}_2\text{O}^+ \tilde{A}^2A_1 - \tilde{X}^2B_2$ emissions at collision energies below 15 eV show that long-range charge-transfer processes populate primarily three A -state bending vibrational levels at or below resonance with $\text{Kr}^+ (^2P_{1/2}) + \text{H}_2\text{O}$ reactants. This is in good agreement with semiclassical models based on energy resonance and Franck–Condon arguments.^{1,2,41}

ACKNOWLEDGMENT

This work is supported by AFOSR under Task No. 2303EP2.

¹E. A. Gislason and G. Parlant, *Comments At. Mol. Phys.* **19**, 157 (1987).

²E. A. Gislason, G. Parlant, and M. Sizun, in *State-Selected and State-to-State Ion–Molecule Reaction Dynamics Part II*, edited by M. Baer and C. Y. Ng (Wiley, New York), *Adv. Chem. Phys.* **82** (1992) 321.

³R. A. Dressler, J. A. Gardner, R. H. Salter, F. J. Wodarczyk and E. Murad, *J. Chem. Phys.* **92**, 1117 (1990).

⁴J. A. Gardner, R. A. Dressler, R. H. Salter, and E. Murad, *Chem. Phys. Lett.* **181**, 5 (1991).

⁵R. A. Dressler, J. A. Gardner, R. L. Lishawa, R. H. Salter, and E. Murad, *J. Chem. Phys.* **93**, 9189 (1990).

⁶R. A. Dressler, J. A. Gardner, R. H. Salter, and E. Murad, *J. Chem. Phys.* **96**, 1062 (1992).

⁷R. A. Dressler, R. H. Salter, and E. Murad, *Planet. Space Sci.* **40**, 1695 (1992).

- ⁸R. A. Dressler, R. H. Salter, and E. Murad, Chem. Phys. Lett. **204**, 111 (1993).
- ⁹R. A. Dressler, R. H. Salter, and E. Murad, J. Chem. Phys. **99**, 1159 (1993).
- ¹⁰R. A. Dressler and E. Murad, J. Chem. Phys. **100**, 5656 (1994).
- ¹¹R. A. Dressler, J. A. Gardner, D. L. Cooke, and E. Murad, J. Geophys. Res. **96**, 13795 (1991).
- ¹²R. A. Dressler and E. Murad, in *Unimolecular and Bimolecular Ion-Molecule Reaction Dynamics*, Wiley Series in Ion Chemistry and Physics, edited by C. Y. Ng, T. Baer, and I. Powis (Wiley, New York, 1994).
- ¹³D. W. Turner, C. Baker, A. D. Baker, and C. R. Brundle, *Molecular Photoelectron Spectroscopy* (Wiley-Interscience, London, 1970).
- ¹⁴J. E. Reutt, L. S. Wang, Y. T. Lee, and D. A. Shirley, J. Chem. Phys. **85**, 6928, (1986).
- ¹⁵R. N. Dixon, G. Duxbury, J. W. Rabelais, and L. Åsbrink, Mol. Phys. **31**, 423 (1976).
- ¹⁶N. G. Adams and D. Smith, in *Techniques for the Study of Ion-Molecule Reactions*, Tech. of Chem., Vol. 20, edited by J. M. Farrar and W. H. Saunders, Jr. (Wiley, New York, 1988).
- ¹⁷T. Su and M. T. Bowers, Int. J. Mass. Spectrom. Ion Phys. **12**, 347 (1973).
- ¹⁸T. Su and M. T. Bowers, J. Chem. Phys. **58**, 3027 (1973).
- ¹⁹D. R. Bates, Chem. Phys. Lett. **82**, 396 (1981).
- ²⁰D. R. Bates, Proc. R. Soc. London, Ser. A **384**, 289 (1982).
- ²¹D. R. Bates, Chem. Phys. Lett. **111**, 428 (1984).
- ²²T. Su, J. Chem. Phys. **100**, 4703 (1994).
- ²³D. Gerlich, J. Chem. Phys. **90**, 127 (1989).
- ²⁴D. Gerlich, in *State-Selected and State-to-State Ion-Molecule Reaction Dynamics*, Adv. Chem. Phys., 82, Part I, edited by M. Baer and C. Y. Ng (Wiley, New York, 1992).
- ²⁵G. A. Fisk, J. D. McDonald, and D. R. Herschbach, Discuss. Faraday Soc. **44**, 228 (1967).
- ²⁶M. K. Bullitt, C. H. Fisher, and J. L. Kinsey, J. Chem. Phys. **60**, 478 (1974).
- ²⁷W. H. Press, B. P. Flannery, S. A. Teukolsky, and W. T. Vetterling, *Numerical Recipes* (Fortran Version) (Cambridge University, New York, 1989).
- ²⁸H. Lew, Can J. Phys. **54**, 2028 (1976).
- ²⁹Ch. Jungen, and A. J. Merer, Mol. Phys. **40**, 1, 25, 40 (1980).
- ³⁰M. Brommer, B. Weiss, B. Folmeg, P. Rosmus, S. Carter, N. C. Handy, H. J. Werner, and P. J. Knowles, J. Chem. Phys. **98**, 5222 (1993).
- ³¹R. A. Dressler, S. T. Arnold, and E. Murad, J. Chem. Phys. **102**, 3481 (1995).
- ³²J. A. Gardner, R. A. Dressler, R. H. Salter, and E. Murad, J. Chem. Phys. **97**, 2473 (1992).
- ³³A. Ding, K. Lacmann, and A. Henglein, Ber. Berl. Bunsenges. Phys. Chem. **71**, 596 (1967).
- ³⁴A. Henglein and K. Lacmann, Adv. Mass Spectrom. **3**, 331 (1966).
- ³⁵K. Lacmann and A. Henglein, Ber. Berl. Bunsenges. Phys. Chem. **69**, 292 (1965).
- ³⁶W. R. Gentry, E. A. Gislason, Y. T. Lee, B. H. Mahan, and C. W. Tsao, Disc. Faraday Soc. **44**, 137 (1967).
- ³⁷J. L. Elkind and P. B. Armentrout, J. Chem. Phys. **84**, 4862 (1986).
- ³⁸H.-S. Kim, C.-H. Ku, and M. T. Bowers, J. Chem. Phys. **93**, 5594 (1990).
- ³⁹Th. Glenewinkel-Meyer and Ch. Ottinger, J. Chem. Phys. **100**, 1148 (1994).
- ⁴⁰Y. Shiraishi and I. Kusunoki, J. Chem. Phys. **87**, 6530 (1987).
- ⁴¹E. Bauer, E. R. Fisher, and G. R. Gilmore, J. Chem. Phys. **51**, 4173 (1969).
- ⁴²Ch. Ottinger, J. Reichmuth, S. Zimmerman, I. Kusunoki, and Y. Shiraishi, J. Chem. Phys. **97**, 9138 (1992).
- ⁴³I. Kusunoki and T. Ishikawa, J. Chem. Phys. **82**, 4991 (1985).
- ⁴⁴J. C. Light, J. Chem. Phys. **40**, 3221 (1964).
- ⁴⁵J. C. Light and J. Lin, J. Chem. Phys. **43**, 3209 (1965).
- ⁴⁶P. Pechukas and J. C. Light, J. Chem. Phys. **42**, 3281 (1965).
- ⁴⁷M. R. Spalburg, J. Los, and E. A. Gislason, Chem. Phys. **94**, 327 (1985).